The 2022 M_W 6.0 Gölyaka-Düzce earthquake: an example of a medium size earthquake in a fault zone early in its seismic cycle

P. Martínez-Garzón[1], D. Becker[1], J. Jara[1], X., Chen[1], G. Kwiatek[1] and M. Bohnhoff[1,2]

[1] Helmholtz Centre Potsdam GFZ German Research Centre for Geosciences, Potsdam, Germany.

[2] Free University Berlin, Institute of Geological Sciences, Berlin, Germany

Corresponding author: Patricia Martínez-Garzón (patricia@gfz-potsdam.de)

Abstract

On November 23rd 2022, a M_W 6.0 earthquake occurred in direct vicinity of the M_W 7.1 Düzce earthquake that ruptured a portion of the North Anatolian Fault in 1999. The M_w 6.0 event was attributed to a small portion of the Karadere Fault off the main North Anatolian Fault that did not rupture during the 1999 sequence. We analyze the spatio-temporal evolution of the M_W 6.0 Gölyaka-Düzce seismic sequence at various scales and resolve the source properties of the mainshock. Modeling the decade-long evolution of background seismicity of the Karadere Fault employing an Epistemic Type Aftershock Sequence model shows that this fault was almost seismically inactive before 1999, while a progressive increase in seismic activity is observed from 2000 onwards. A newly generated high-resolution seismicity catalog from 1 month before the mainshock until six days after created using Artificial Intelligence-aided techniques shows only few events occurring within the rupture area within the previous month, no spatio-temporal localization process and a lack of immediate foreshocks preceding the rupture. The aftershock hypocenter distribution suggests the activation of both the Karadere fault which ruptured in this earthquake as well as the Düzce fault that ruptured in 1999. First results on source parameters and the duration of the first P-wave pulse from the mainshock suggest that the mainshock propagated eastwards in agreement with predictions from a bimaterial interface model. The M_W 6.0 Gölyaka-Düzce event represents a good example of an earthquake rupture with damaging potential within a fault zone that is in a relatively early stage of the seismic cycle.

Key Points

- Increased seismicity observed for Karadere fault after 1999 M_W 7.4 Izmit earthquake while almost seismically inactive before.
- Aftershock distribution suggests activation of both the Karadere fault rupturing in this earthquake and Düzce fault that ruptured in 1999.
- Characteristics of P-wave first pulses suggest eastward rupture propagation in agreement with predictions from bimaterial interface models.

1. Introduction

Large strike-slip fault zones such as the San Andreas Fault in California, USA, or the North Anatolian Fault in Türkiye, among others, host some of the largest shallow earthquakes (typically up to M ~ 8, see e.g. Wesnousky et al., 1988; Stirling et al., 1996; Martínez-Garzón et al., 2015) worldwide. Some of these hazardous faults run near urban areas, and hence they have an associated risk. This is the case of the western portion of the North Anatolian Fault, being a seismic threat for the Istanbul metropolitan area and nearby population centers. There, the return period of M > 7 earthquakes rupturing the main fault trace has been estimated to be approximately 250 years

(Murru et al, 2016). The most recent large earthquakes along the NAFZ were the August 17th 1999 MW 7.4 Izmit and the November 11th,1999 MW 7.1 Düzce events (Fig. 1). Together they ruptured approximately 180 km and connected the Marmara segment in the west to the 1944 rupture in the east (Bürgmann et al., 2002; Sengör et al., 2005; Bohnhoff et al., 2013). On Nov 23rd 2022, a M_W 6.0 earthquake occurred around 6 and 10 km away from the cities of Gölyaka and Düzce, respectively, and about 200 kilometers eastward of the Istanbul metropolitan area. In the following, we refer to this event as the Gölyaka-Düzce earthquake, felt especially in the province of Düzce and its districts (Eyidogan, 2022). Hypocenter locations provided by KOERI[1] and AFAD[2] reported that the Gölyaka-Düzce earthquake occurred close to the intersection of the ruptures of the 1999 MW 7.4 Izmit and MW 7.1 Düzce earthquake ruptures (Bouin et al., 2004; Konca et al., 2010, Fig. 1). Such M ~ 6 earthquakes are relatively infrequent in the region (according to the ISC-GEM[3] catalog, similar size events could have occurred in 1926 and 1944) but they hold potential to damage key infrastructure and lead to casualties. Hence, analyzing this earthquake and its pre- and post- seismic deformation is important to illuminate the local fault architecture (e.g. Ross et al., 2020), and recover how moderate events nucleate in the region (e.g. Malin et al., 2018; Durand et al., 2020). In addition, analysis of the earthquake source properties can help to decipher any preferential directions of seismic energy release, which is essential for seismic hazard estimation.

The Gölyaka-Düzce earthquake was the first M ~ 6 in the area after the 1999 M > 7 earthquakes and their aftershock sequences. As such, it represents the occurrence of an earthquake with damaging potential in a fault zone that is broadly still in the early stage of the seismic cycle, when the accumulated elastic strain is relatively low. However, at this location, the geometry of the fault zone is highly complex, with slip partitioning along two main fault traces bounding the Almacık Block and numerous secondary faults obliquely oriented (Fig 1c). Moment tensor estimation by different agencies (Table S1) consistently reported on a strike-slip mechanism with a small normal faulting component for this earthquake. The hypocenter location and fault plane appeared consistent with a portion of the Karadere Fault (Fig 1c). Different lines of evidence suggest that a at least a few km of the Karadere Fault did not rupture during the 1999 Izmit-Düzce sequence and thus remained loaded and then ruptured in the Gölyaka-Düzce earthquake (Bohnhoff et al., 2016b, Özalp and Kürcer, 2022). These include (i) the magnitude of the latest mainshock, (ii) the spatial extension of aftershocks and (iii) the previous surface mapping of local faults. First field surveys immediately after the M_W 6.0 Gölkaya-Düzce earthquake found no surface rupture indicating that the slip did not extend to the surface (Özalp and Kürcer, 2022).

In this study, we analyze the spatio-temporal evolution of the Gölyaka-Düzce seismic sequence and the preceding seismicity in the area in detail with a focus on the source mechanisms and in context of the local seismotectonic setting. Our primary goals are to determine how the earthquake initiated, what are the ongoing deformation mechanisms in the region, and how the energy from this mainshock was radiated. Insights from this earthquake sequence are important to learn about the dynamics of potentially damaging earthquakes in complex transform fault settings, and the

[1] Kandili Observatory and Earthquake Research Institute. http://www.koeri.boun.edu.tr/new/en
[2] Disaster and Emergency Management Presidency https://www.afad.gov.tr/
[3] ISC-GEM: International Seismological Centre http://www.isc.ac.uk/iscgem/

rupture of highly stressed faults in immediate vicinity to a major strike-slip transform with relatively low stress conditions corresponding to the fault zone being early in its seismic cycle.

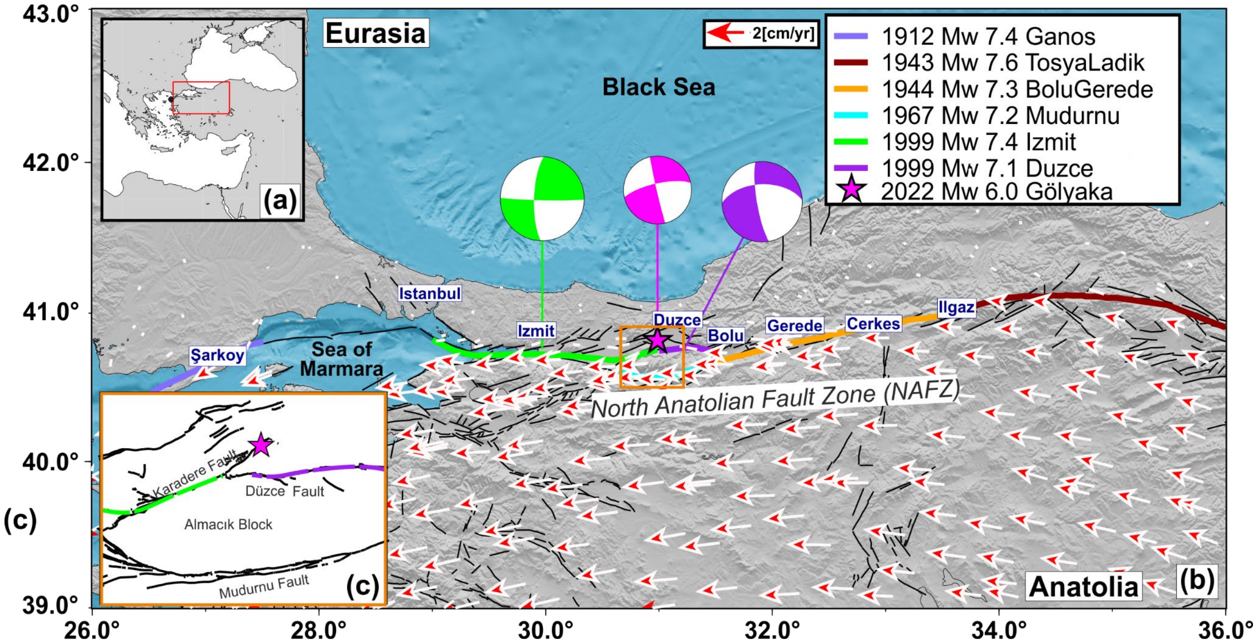

__Figure 1: Seismotectonic setting.__ (a) Location map with red rectangle indicating the area enlarged in (b). The small black circle represents the location of the 2014 M 6.9 Saros earthquake. (b) Study area with the location of main population centers along the North Anatolian fault zone (NAFZ). Colored lines denote rupture extents of historical earthquakes along NAFZ, with their respective magnitudes and dates indicated in the legend. Arrows are an updated GPS velocity field for Türkiye (Kurt et al., 2022), considering the Eurasia-fixed reference frame. The magenta star indicates the Gölyaka earthquake epicenter along with its focal mechanism from KOERI, as well as the focal mechanisms of the Izmit (green) and Düzce (purple) earthquakes in 1999 (data from the global CMT catalog, Ekström et al., 2012; Dziewonski et al., 1981. (c) into the region struck by Gölyaka earthquake.

2. Data and Methodology applied

2.1 Background seismicity evolution

To put the Gölkaya-Düzce seismic sequence in a regional and long-term context, we established a consistent regional seismicity catalog between 1990 and 2022 for the two national seismic agencies. The AFAD catalog has 31,081 events with magnitudes M [1.3 - 7.6] for such a period, whereas the KOERI catalog reported 42,050 events M [1.4 - 7.4]. We analyzed the decade-long evolution of the AFAD and KOERI regional seismicity catalogs through a declustering process (Fig. 2). Both catalogs changed the reported magnitude type at the end of 2011 and beginning of 2012, from duration magnitude M_d to local M_L. For consistency we homogenized both catalogs converting uniformly to moment magnitude M_W, following the empirical relationships proposed for the study region by Kadirioglu & Kartal (2016):

$$M_W = 0.7949M_d + 1.3420, \quad (1)$$

$$M_W = 0.8095 M_L + 1.303. \tag{2}$$

After both catalogs were homogenized to M_W, we estimated the magnitude of completeness M^C of each catalog, following a probabilistic approach to fit the frequency-magnitude curve (Ogata and Katsura, 1993; Daniel et al., 2008, Jara et al., 2017). In contrast to the maximum curvature method, this technique fits a function to explain the magnitude-frequency distribution, including all catalog events. The number of earthquakes is fit as a function of magnitude as follows:

$$N(m) = A \times 10^{-bm} \times q(m), \tag{3}$$

where the b-value represents the slope of the Gutenberg-Richter law, A is a normalization constant, and $q(m)$is the probability that one earthquake of magnitude $m$is listed in the catalog . Then, we modeled q as (Ogata and Katsura, 1993):

$$q(m) = \frac{1}{2} + \frac{1}{2} erf\left(\frac{m-\hat{\mu}}{\sqrt{2}\hat{\sigma}}\right), \tag{4}$$

where erf is the error function and $\hat{\mu}$ and $\hat{\sigma}$ correspond to the mean and standard deviation of the probability distribution function, respectively. We optimized $[A, b, \hat{\mu}, \hat{\sigma}]$ for each catalog following a Bayesian approach to derive the parameters posterior Probability Density Function (PDF). We used the Markov Chain Monte Carlo sampler of PyMC (Salvatier et al., 2016), to draw 500.000 samples from the posterior PDF. The inferred parameters and their associated uncertainties are in Table S2. Then, the completeness magnitude M^C is computed as follows:

$$M^C = \hat{\mu} + 2\hat{\sigma}, \tag{5}$$

i.e., a 97.7% probability threshold, which yielded a $M^C = 3.4$ for the AFAD catalog, whereas, for the KOERI one, we obtained a $M^C = 4.1$ (see insets in Fig 2, and Figs S1 and S2 for the obtained fitting). Once M^C was estimated for both catalogs, we declustered them using an epidemic-type aftershock sequence model (Marsan et al., 2017; Jara et al., 2017). Such approach considers the total seismicity rates $\lambda(x, y, t)$ as the following sum:

$$\lambda(x, y, t) = \mu(x, y, t) + \nu(x, y, t), \tag{6}$$

where $\nu(x, y, t)$ accounts for the aftershock productivity, and $\mu(x, y, t)$ is the background seismicity rate for earthquakes occurring at a given location (x, y) and time t. The aftershock rate was estimated following the Omori-Utsu law pondered by a power spatial density, following:

$$\nu_i(x, y, t) = \sum_{i \vee t_i < t} \frac{\kappa(m_i)}{(t+c-t_i)^p} \frac{(\gamma-1)L(m_i)^{\gamma-1}}{2\pi\left((x-x_i)^2+(y-y_i)^2+L_i^2\right)^{\frac{\gamma+1}{2}}}, \tag{7}$$

in which c, γ, and p are constants, and $\kappa(m)$ is the productivity law with a constant α [Ogata, 1988]. $L(m) = L_0 \times 10^{0.5(m-M^C)}$ is the characteristic length in km (Utsu & Seki, 1955; van der Elst & Shaw, 2015). Here, we imposed realistic values for parameters $\alpha = 2$, $p = 1$, $c = 10^{-3}$ days, $\gamma = 2$, and $L_0 = 1.78$ km (Marsan et al., 2017; Jara et al., 2017; Karabulut et al., 2022). Parameters κ and $\mu(x, y, t)$ were inverted. The background seismicity was computed as follows:

$$\mu(x,y,t) = \sum_i \frac{\mu(x_i,y_i,t_i)}{\lambda(x_i,y_i,t_i)} e^{\frac{-\sqrt{(x-x_i)^2+(y-y_i)^2}}{l}} e^{-t-t_i\sqrt{\tau}} \times \frac{1}{2\pi l^2 a_i}, \tag{8}$$

with l and τ space and time being smoothing parameters, and $a_i = 2\tau - \tau\left(e^{\frac{t_s-t_i}{\tau}} - e^{\frac{t_e-t_i}{\tau}}\right)$, where t_s and t_e are the temporal beginning and end of the catalog, respectively. κ is inferred as:

$$\kappa = \frac{\sum_i \quad 1-\frac{\mu(x_i,y_i,t_i)}{\lambda(x_i,y_i,t_i)}}{\sum_i \quad e^{\alpha m_i}(ln(t_e+c-t_i)-ln(c))}. \tag{9}$$

Here, we used a smoothing length l =100 km and a smoothing duration τ = 100 days. Such choices are able to preserve the potential accelerations/decelerations from catalogs (Marsan et al., 2017; Jara et al., 2017). We declustered the catalogs using the obtained M^C for each catalog and the fault regions in Fig 2. When doing so, we observed an apparent increase in the seismicity from the AFAD declustered catalog around 2012 (Fig S1). Around that time, AFAD changed the reported magnitudes from M_d to M_L. Although we converted the corresponding magnitudes to M_W, this change in the magnitude estimation might still produce spurious acceleration/deceleration in the background seismicity rate. We then tested higher M^C values, finding that such behavior disappears around M^C = 4.1 (Fig S1). Thus, we finally used M^C = 4.1 for both catalogs (Fig 3a, b). The final parameters utilized for each catalog are provided in Table S1.

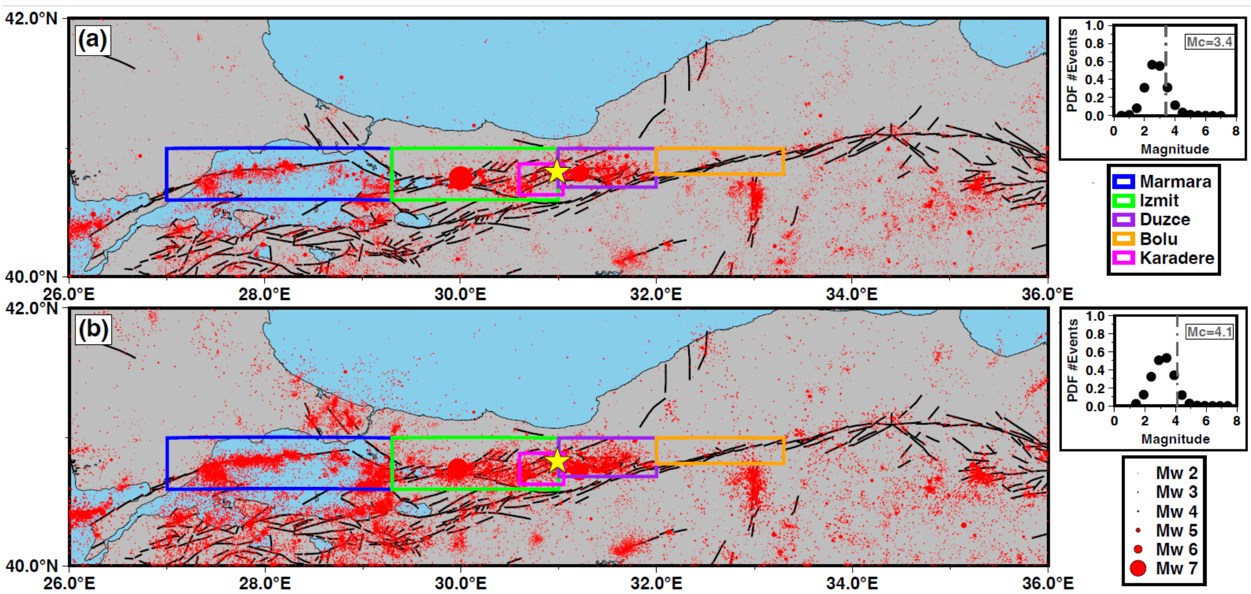

Figure 2: ***Regional Seismicity****. (a) AFAD catalog from 1990 to 30/11/2022. Yellow star denotes the M*$_W$ *6.0 Gölyaka-Düzce epicenter. Color boxes indicate the target regions where the seismicity is analyzed. Right:Catalog's Probability Distribution Function (PDF), where the vertical dashed line denotes the M*^{C}*. (b) Same as (a), but for KOERI catalog. See Figs. S3 and S4 for the spatial distribution of seismicity inside each region.*

2.2 Enhanced seismicity catalog framing the mainshock

To generate an optimized enhanced seismicity catalog with lowest possible magnitude detection threshold around the M_W 6.0 Gölkaya-Düzce earthquake epicenter, we processed continuous waveform recordings from 16 local seismic stations and 9 local accelerometer stations. We covered a time period from one month before the mainshock up to almost 6 days after it (October 23rd, 2022 at 00:00h up to November 29th, 2022 at 00:00h. The employed stations belong to the AFAD and KOERI seismometer and strong motion networks.

We detected P- and S- wave onset times embedded in the continuous recordings applying the supervised Artificial Intelligence method Phasenet (Zhu and Beroza, 2019) trained on the seismicity database from Northern California. This method has proven to improve the detection process especially of small earthquakes (e.g. Martinez-Garzon et al., 2023). With this method, 148,948 body wave onsets were detected, out of which 78,410 were detections of P-waves and 70,568 were detections of S-waves.

The P- and S- picks were associated with seismic events using the unsupervised technique GAMMA (Zhu et al., 2022). To classify an event to be an earthquake, a minimum of 4 necessary picks (either P and/or S) was set. The picks were spatio-temporally clustered using the Density Based Spatial Clustering of Applications with Noise (DBSCAN) method. About 19% of the total amount of picks were associated with earthquakes. This way, we have obtained a catalog of detections containing 3,361 possible seismic events (Fig 3a).

As a comparison, KOERI reported a total of 505 events with magnitudes $\geq M_L$ 0.5 for the same spatio-temporal region analyzed here (Fig 3b). Out of them, 440 correspond to common events from both catalogs.

In the next step, the waveforms from all events corresponding to the period before the M_W 6.0 mainshock were visually inspected. About 343 detections from the time period before the mainshock were removed as they showed signals in only one or two of the accelerometers, typically exhibiting $t_S - t_P > 5\ s$, which is larger than what is expected for a small local event. Additional 35 events were identified as regional events with locations outside the study region, and additional 11 events were identified as duplicates and removed. In the following, we refer to this catalog as the "*catalog of detections*".

We calculated event locations by employing the probabilistic location software NLLoc (Lomax et al., 2000; 2009). Here, only events with a minimum of 6 P- and/or S- picks were further processed, which implicitly removes possible false signal associations with less than 6 phases from the catalog of detections. The local 1-D velocity model from Bulut et al. (2007) was employed assuming a constant v_p/v_s ratio of 1.73. The search area encompassed a 400 km x 200 km region centered around the mainshock epicenter. In the following, we refer to this refined catalog as the "*catalog of absolute locations*". Further details on the refining of the catalog of absolute locations are provided in Text S1. This way, we obtained a catalog of 1,290 events with absolute locations, containing 8,927 P-wave picks and 7,822 S-wave picks for further processing (Fig. S5). In this catalog, the median errors in the x-, y- and z- directions are 2.3 km, 3.1 km and 3.4 km, respectively.

In the next step, a relative event relocation was performed using hypoDD (Waldhauser & Ellsworth, 2000; Waldhauser et al., 2004). We utilized both catalog differential travel times derived from the automatic Phasenet P- and S-picks and cross-correlation time differences derived from the event waveforms. To estimate the waveform cross-correlations, we employed time windows covering 1 s and 2 s centered at the P- and S-onset, respectively. The waveforms were filtered with a 3rd order Butterworth bandpass filter between 2 and 10 Hz. The retrieved correlations with a normalized cross-correlation coefficient of at least 0.7 were kept and the square of the cross correlation coefficient was used as weight in the relocation procedure. To look at the spatio-temporal evolution of the seismicity, we demanded a minimum of 8 catalog time differences (either P- and/or S-phases) for each event combination resulting in a catalog of 918 relocated events. In the following, we refer to this further refined subset as the "*relocated catalog*". The median formal relative relocation errors in the x-, y-, and z- directions are 11 m, 13 m, and 12 m, respectively.

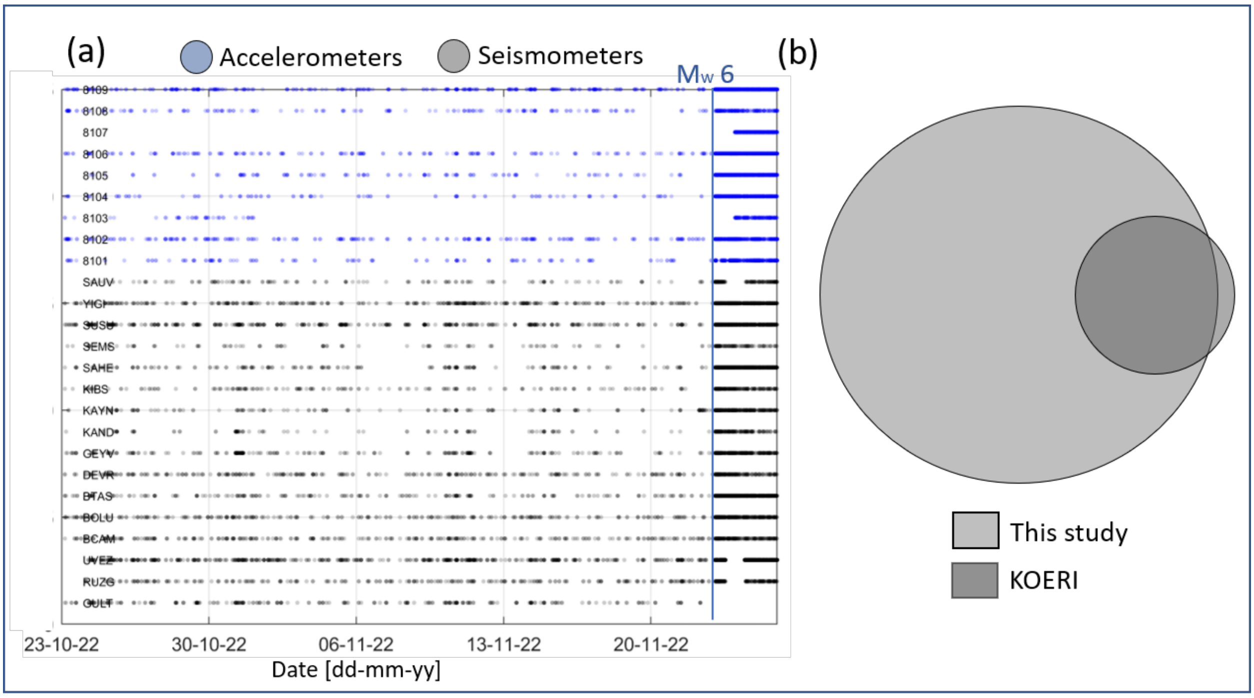

***Figure 3: Picks and detections from the AI-aided catalog**. (a) Associated picks as a function of time, per station. Vertical blue line marks the M_W 6.0 Gölyaka-Düzce earthquake. (b) Venn diagram showing the earthquakes included in our catalog of detections vs the events included in the KOERI catalog for the same spatio-temporal region.*

2.3 Earthquake source parameters and directivity

The estimation of point source parameters of the M_W 6.0 mainshock was performed using the spectral fitting method (Kwiatek et al., 2015). We used 249 high-gain seismometers of Kandilli Observatory (KO) and the National Seismic Network of Türkiye (TU). The combination of these networks offers sufficient azimuthal coverage and signal-to-noise ratio for the analyzed catalog. From these networks, stations with epicentral distances of 200 - 800 km are used to derive source parameters of the mainshock.

Three-component ground velocity waveforms from stations with a signal-to-noise ratio of at least 4 dB were filtered using a 2nd order 0.02 Hz high-pass Butterworth filter and then integrated in the time domain. We utilized window lengths of 25 s from the P- and S- wave ground displacements, allowing for additional 4 s before the P- or S- wave onsets. The selected window length of 25s in combination with the minimum station distance of 200 km prevents contamination of the P-wave window by S-wave energy as the S-P time difference is larger than 25 seconds assuming average velocities and vp/vs-ratios along the travel path. The edges of the selected windows were smoothed using von Hann's taper. We utilized the three components from the far-field ground displacement spectra using the Fourier transform and then combined altogether. The observed ground displacement spectra were fit to Brune's point-source model expressed as:

$$u^{th}(f) = \frac{\langle R_C \rangle}{4\pi\rho {V_C}^3 R} \frac{M_0}{1+\left(\frac{f}{f_C}\right)^2} exp\left(\frac{-\pi f R}{V_c Q_c}\right), \quad (10)$$

where R is the source-receiver distance, M_0 is the seismic moment, f_c is the corner frequency where c represents either the P- or S- wave, Q_c is the quality factor, and $< R_c >$ is the average radiation pattern correction coefficient of either P- or S- waves. Following Boore and Boatwright (1984), we applied R_P=0.65 and R_S=0.7 for P and S waves, respectively, that are representative constants for the regional strike-slip faults. We used V_P = 5680 m/s and V_S = 3280 m/s (from Bulut et al., 2007, averaged at the depth interval where the earthquakes occurred), assuming V_P/V_S = 1.73 and a density ρ = 2700 kg/m^3. We inverted for [M_0, f_c, Q_c] optimizing the cost function:

$$\|log_{10}u^{obs}(f) - log_{10}u^{th}(f)\|_{L1} = min, \quad (11)$$

where $u^{th}(f)$ and u^{obs} are the theoretical and observed ground displacement amplitude spectrum for a given station and P or S wave. The starting model for M_0 and f_c was taken using Snoke's integrals (Snoke, 1987) and we assumed initial values of Q = 400 for both P- and S- wave trains. We utilized a grid search optimization (assuming starting model) followed by simplex algorithms (starting from the best model of a grid search). Source parameters that deviated from the average by more than three standard deviations were eliminated from the calculation. The final source parameters (i.e. seismic moment, corner frequency, quality factor) were calculated as average values from all stations.

In the following, we calculated the static stress drop using the formula valid for a rectangular strike-slip fault (Shearer 2009):

$$\varDelta\sigma = \frac{2}{\pi} \frac{M_0}{W^2 L}, \quad (12)$$

where $W=8$ *km* represents the fault width, assumed from the depth extent of the aftershocks (see Section 3.2.2). The rupture length L is estimated as double the source radius while using Brune's source model constants and, for comparison, the Haskell's rectangular source assuming V_R=0.9V_s (see Savage et al., 1972, Table 1 for details) using the equation

$$L = \frac{C_C V_C}{2\pi f_c} \quad (13)$$

in which C_C is the geometrical correction coefficient (C_P= C_S = 4.7 for Brune's model, and C_P = 1.2, C_S = 3.6 for the Haskell's model, see Savage et al., 1972) and f_C and V_C represent the corner frequency and seismic velocity of either P- or S-waves, respectively.

For the earthquakes comprising the absolute locations catalog, we estimated only moment magnitudes M_W using a simplified approach following Snokes's (1987) integrals:

$$J_S = 2\int [u^{\cdot}(f)]^2 df, \quad (14)$$

$$K_S = 2\int [u(f)]^2 df, \quad (15)$$

where $u^{\cdot}(f)$ and $u(f)$ are ground velocity and displacement S-wave spectra corrected for attenuation and prepared from S-wave waveforms processed in the same way as for the mainshock. The original seismograms were filtered with 1 Hz high-pass 2nd order Butterworth filter and we used a shorter 5 s window framing the first S-wave arrival to limit the influence of low-frequency noise for predominantly small earthquakes (M<4). The integrals in eq. (14) and (15) were corrected for the finite frequency band following di Bona and Rovelli (1991). The seismic moment has been estimated with (Snoke, 1987):

$$M_0 = 8\pi\rho {V_S}^3 R \left(\frac{{K_S}^3}{J_S}\right)^{0.25}, \tag{16}$$

and the moment magnitude was calculated using the standard relation (Hanks and Kanamori, 1976):

$$M_W = \frac{(log_{10}M_0 - 9.1)}{1.5}. \tag{17}$$

Similar to the mainshock, for each event the final seismic moment and moment magnitude were calculated as average values from all stations containing S-wave arrivals. Due to the limited number of S-waves with sufficient signal-to-noise ratio for the smallest earthquakes, the uncertainties were estimated using the mean absolute deviation.

Large earthquake ruptures potentially involve a propagation process along a fault plane. The rupture propagation direction could be deduced from the azimuthal variations of amplitude and frequency content of the apparent source time functions (ASTF) (Stein and Wysession, 2003) providing important information for seismic risk assessment. For a unilateral rupture, ideally this would lead to shorter ASTFs displaying larger amplitudes in the direction of rupture propagation, and longer duration and smaller amplitude ASTFs in the opposite direction. To obtain the ASTFs, we initially tested the application of Empirical Green's Function (EGF) technique and tried four EGF candidates (Table S3) to recover the directivity of the mainshock (see text S2 for all details) that led to inconclusive results.

We therefore tested the azimuthal variations in the duration and frequency content of the initial P-wave arrivals for seismometers located at epicentral distances of 50-100 km from the mainshock. For comparison, we additionally included integrated signals from accelerometers located at much closer distances. We only used unclipped first P-wave pulses that were rotated into the radial direction from 3-component seismograms to enhance the signal-to-noise ratio of the initial portions of the P-wave. The first P-wave pulses contain a combination of information including the source time function and effects related to wave propagation. However, comparing P-wave pulse characteristics for stations located at similar distances from the mainshock epicenter allows us to suppress propagation effects. Therefore, the initial portion of the seismogram can be taken as a proxy for the ASTFs. Variation in rise time and duration of the P pulses can then be used to infer whether the earthquake displays rupture directivity.

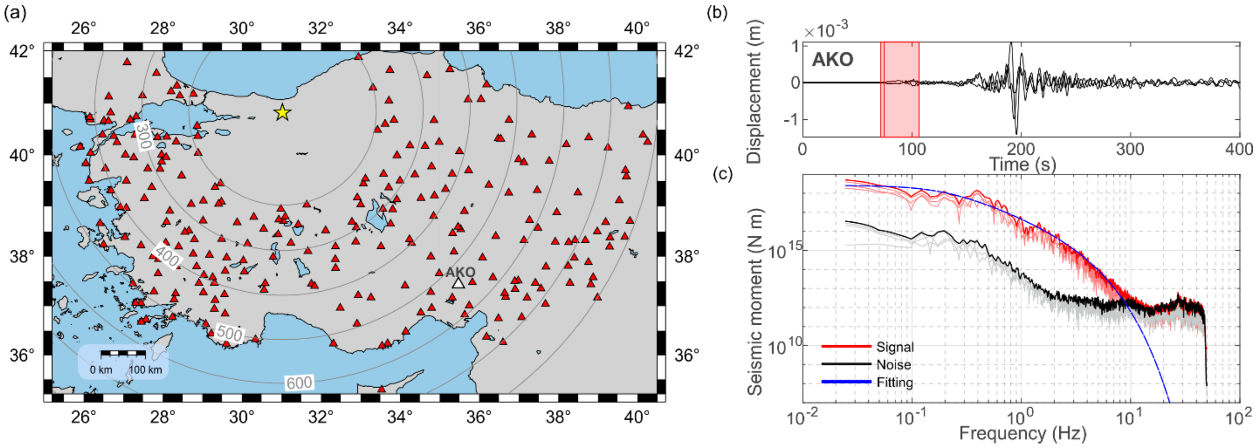

Figure 4. Source parameter analysis. *(a) Station distribution employed for the source parameter estimation (red upward triangles). These stations lie within a source-station distance between 200 km and 800 km. Yellow star shows the 2022 M_W 6.0 Gölyaka-Düzce mainshock. (b) Three-component displacement waveforms for the mainshock recorded by station AKO (with epicentral distance ~530 km, see white triangle in (a)). Red rectangle highlights the employed P-wave window. (c) Displacement spectrum of the P-wave signal (red) and the noise before the signal (black). Blue thick line indicates the modeled spectrum yielding the source parameters:* $M_0 = 2.62 \times 10^{18}, f_c = 0.19Hz, Q_P = 308$.

3 Results

3.1 Long-term evolution of background seismicity in the Gölyaka-Duzce region

We analyzed the evolution of the background seismicity along defined segments of the NAFZ including the Marmara, Izmit, Düzce, Bolu, and Karadere segments (Fig. 2). Both national Turkish catalogs introduced above show that the Bolu segment displays a low background seismicity rate when compared to e.g. Izmit or Marmara segments (Fig 5). Aseismic slip (surface creep) has been reported to occur along this segment, occurring for at least 70 years (Ambraseis, 1970; Cakir et al., 2005; Cetin et al., 2014; Bilham et al., 2016, Jolivet et al., 2023). This might be a possible explanation for the low seismicity rate. The Marmara, Izmit, and Düzce segments appear to host a constant background seismicity rate with time, especially after the 1999 Izmit and Düzce sequence (Fig 5). Both catalogs report a deceleration of background seismicity after the 2014 M_W 6.9 Saros earthquake (Bulut et al., 2018), supporting the idea that some significant deformation process not yet understood in detail was affecting the seismicity along the NAFZ (Karabulut et al., 2022).

The Karadere fault hosted a comparatively low background seismicity before the 1999 Izmit and Düzce earthquake sequence. A change in its seismic behavior is observed afterwards, when this segment experienced an increase of the seismic activity including more than 5 events with M > Mc = 4.1. The shape of the background rates is different for the AFAD and KOERI catalogs. This difference might be due to the different number of seismic stations operated by the agencies in this area, hence affecting the monitoring capabilities and detection thresholds. Therefore, it is likely that the region was tectonically activated by the earthquake sequence in 1999, and progressively loaded since then, leading to the M_W 6.0 Gölyaka-Düzce earthquake 23 years later. Interestingly, the region did not exhibit a lower background rate after the 2014 M_W 6.9 Saros earthquake, different to the other NAFZ segments in the area.

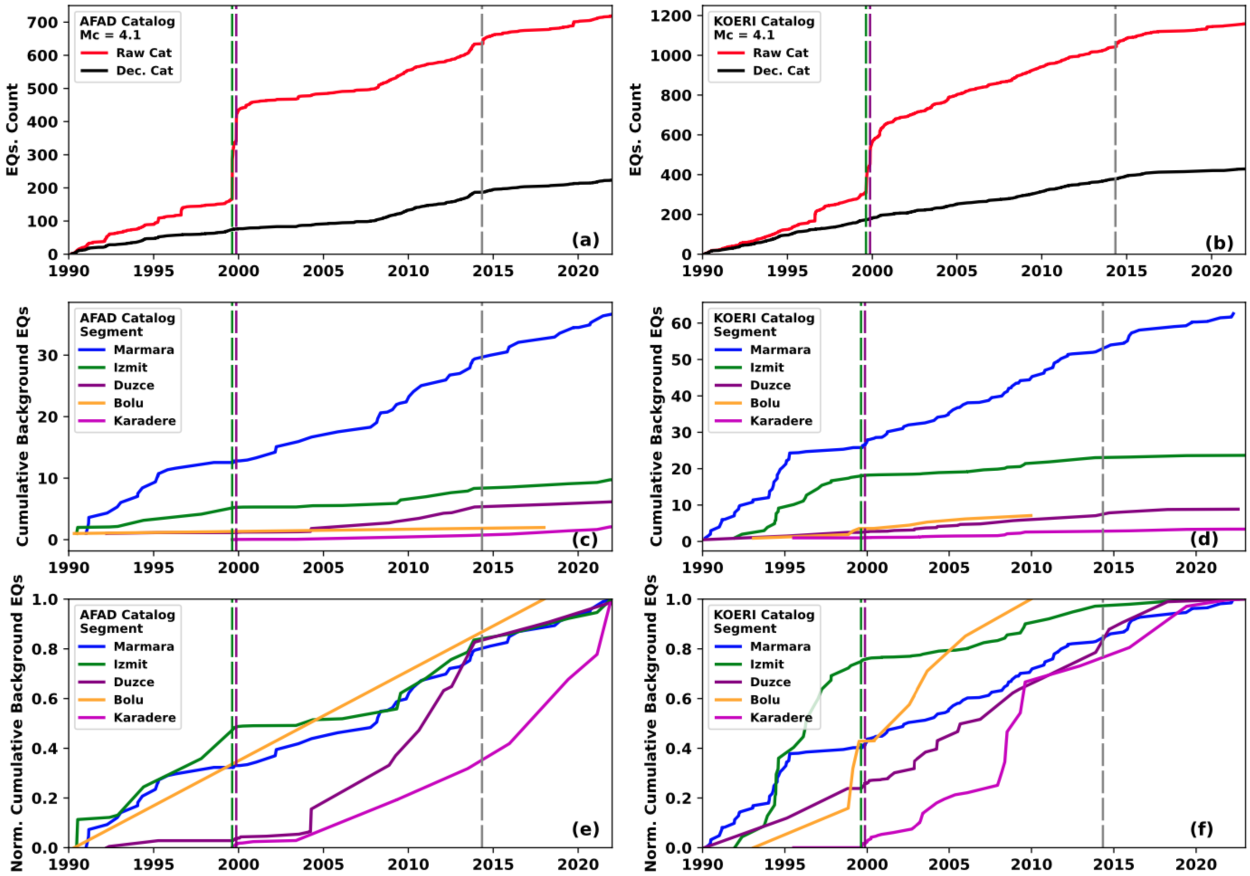

Figure 5: ***Temporal evolution of the background seismicity at different segments of the NAFZ.*** *(a) Complete (black) and declustered (red) AFAD catalog using* M^C*=4.1. (b) Same as (a) but with KOERI catalog. (c) Cumulative background seismicity, color-coded by region as in Fig. 2, for the AFAD catalog. (d) same as (c) for the KOERI catalog. The vertical green, magenta and grey lines represent the time of occurrence of the* M_W *7.4 Izmit,*M_W *7.1 Düzce, and* M_W *6.9 Saros earthquakes, respectively. (e) Normalized cumulative background seismicity, color-coded by region as in Fig. 2, for the AFAD catalog. (d) same as (c) for the KOERI catalog.*

3.2 Spatio-temporal seismicity distribution before and after the 2022 Gölyaka-Düzce earthquake

We obtained an enhanced seismicity catalog with 1,290 refined hypocenter locations as described in Section 2.2 covering the area of longitude [30-32°E] and latitude [40-42°N] for the time period [October 23rd, 2022 at 00:00h up to November 29th, 2022 at 00:00h] and including moment magnitudes as low as M_W 0.7. Out of them, a total of 222 and 1,032 seismic events correspond to events preceding and following the 2022 Gölyaka -Düzce mainshock, respectively. For the same region and time interval, the seismicity catalog provided by the KOERI agency contained 529 events, out of which 23 and 506 corresponded to events preceding and following the mainshock, respectively (Fig 3b).

Using a goodness of fit method (Wiemer and Wyss, 2000), the magnitude of completeness of the derived catalog within selected region is $M_W^c = 1.5$. Calculating the *b*-value for events above M^C, from both the periods before and after the mainshock, we find a value of $b = 0.95 \pm 0.05$ (Fig. S6). This could be related to the fact that we utilized M_W while many other estimates use M_L that may lead to larger *b*-value (see e.g. Raub et al., 2017). Alternatively, the relatively low *b*-value may suggest that the fault did not yet release all its accumulated strain (e.g. Gulia & Wiemer, 2019). Given the magnitude of the mainshock and the spatial extent of the rupture we consider the latter option as rather unlikely.

3.2.1 Seismic activity preceding the Gölyaka-Düzce earthquake

The M_W 6.0 Gölyaka-Düzce earthquake hypocenter is located at the northeastern portion of the Karadere fault that remained unbroken during the 1999 M_W 7.4 Izmit and 1999 M_W 7.1 Düzce events.

The area that ruptured in the M_W 6.0 Gölyaka-Düzce earthquake and its surroundings only displayed a small number of seismic events during the 30 days preceding the mainshock. The catalog of absolute locations reported 222 seismic events during this time, out of which 55 could be successfully relocated. Most of the relocated seismic activity occurred away from the future M_W 6.0 earthquake rupture, extending up to 50 km to the East (Fig. 6). The locations of these seismic events show a good correspondence with the mapped local faults (Emre et al., 2018). A small cluster of events is visible at the eastern edge of the analyzed region, coinciding with the termination of a local fault, near a quarry area (see Fig. 6a for location). The presence of a quarry in the area suggests that some of these events could be quarry blasts. However, these events appear to be regular seismic events based on the following: (i) these detections display regular P- and S-wave trains, (ii) their hypocentral depth is deeper than 8 km, and (iii) these events occur randomly in time. Within a 25 km radius from the epicenter of the M_W 6.0 Gölyaka-Düzce earthquake, 23 events were included in the catalog of absolute locations. The most active time period was between Nov 6th and 11th, where a small spatially clustered seismic sequence with magnitudes up to M_W 2.2 occurred about 7.5 km to the North of the mainshock epicenter (Fig 6, Fig S7). The location of this cluster coincides with the deepest part of the fault activated with the aftershock sequences.

Both the catalog of detections and the catalog of absolute locations show that seismicity rates were time-invariant with a transient increase in seismic activity around Nov 10th reflecting the transient cluster North of the future mainshock. This increase in the seismicity rates quickly decayed back to the level before the occurrence of the cluster, remaining constant until the occurrence of the mainshock (Fig 7). The regional seismicity did not display any significant acceleration at the scale of days to hours before the mainshock.

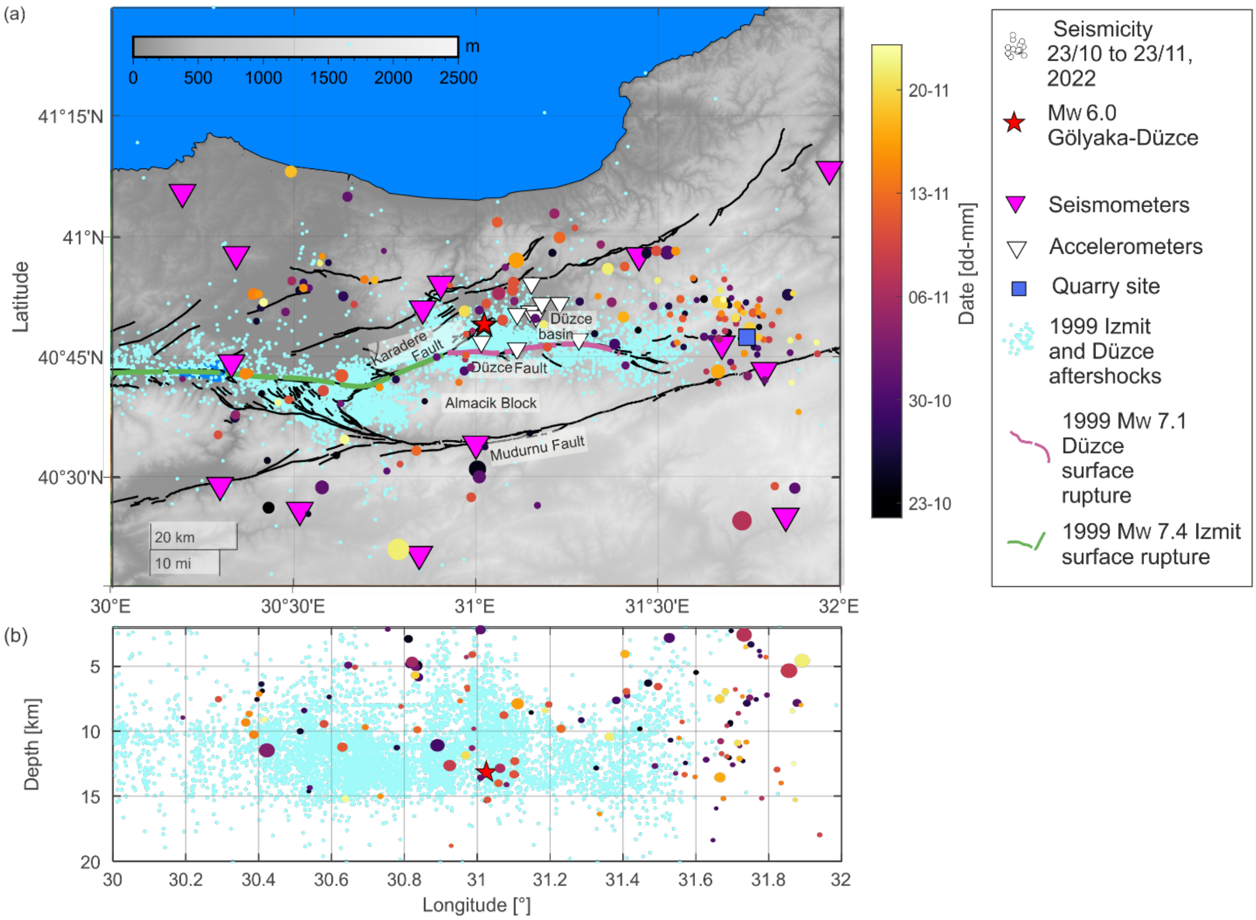

Figure 6: Seismicity located during the preceding month. *Seismicity distribution included in the absolute location catalog (colored circles) during the month preceding the Gölyaka-Düzce earthquake (red star). Symbol size is encoded with magnitude. Surface ruptures of the 1999* M_W *7.4 Izmit and* M_W *7.1 Düzce earthquakes are shown with green and pink dashed lines, respectively. For comparison, seismic activity for three different time periods around the 1999 Izmit and Düzce mainshock is shown in cyan (from Bohnhoff et al, 2016b; Bulut et al., 2005). Fault traces are from Emre et al., (2018).*

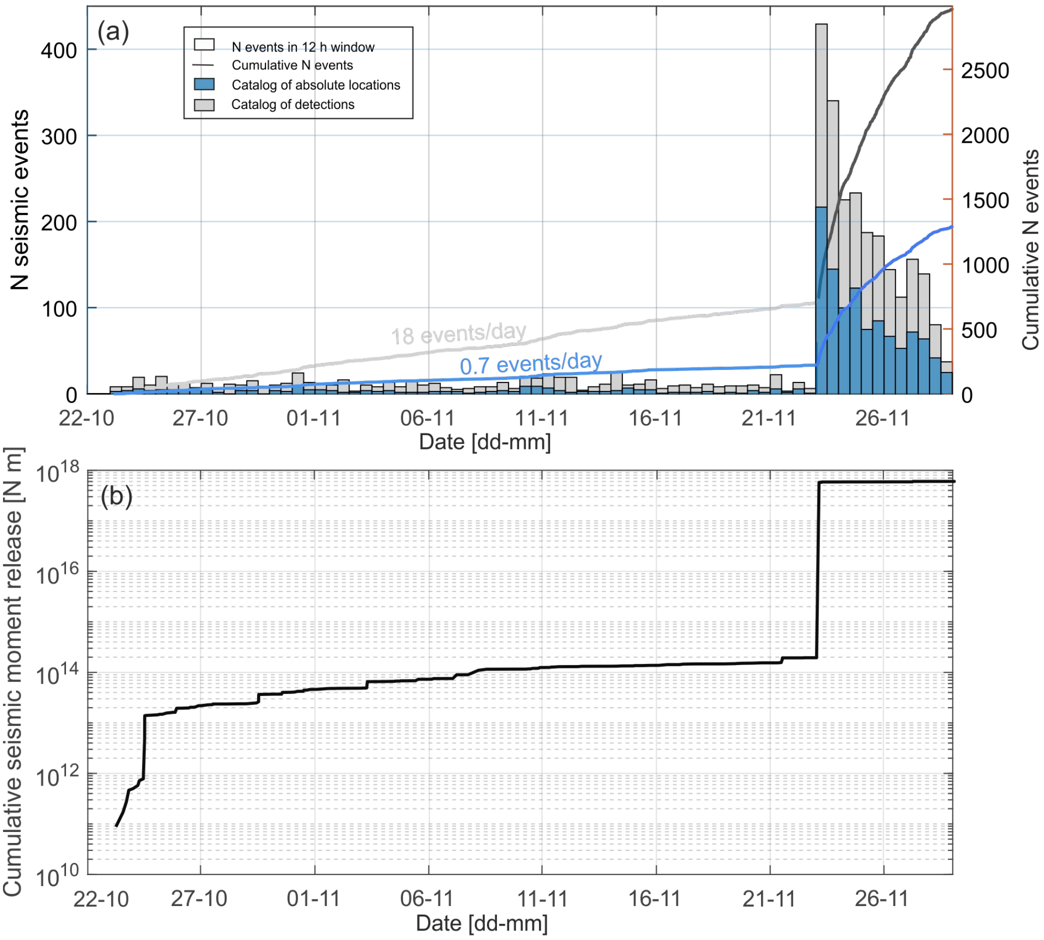

Figure 7: ***Temporal evolution of seismic activity and seismic moment.*** *(a) Bars: Histogram of seismicity rates, where every bar represents a time period of 12h. Grey and blue colors represent the seismicity included in the catalog of detections and absolute locations, respectively. Lines: Cumulative number of seismic events as a function of time. Lighter and darker colors represent the time periods before and after the mainshock (b) Evolution of cumulative seismic moment release from the catalog of absolute locations.*

3.2.2 The aftershock sequence following Gölyaka-Düzce earthquake

After the M_W 6.0 Gölyaka-Düzce earthquake, vigorous seismic activity struck the region during the following days. Compared to the scattered seismicity in a much larger region, most of this early aftershock activity occurs within an area extending 15 km to the East and West as well as 8 km to the North and South of the mainshock epicenter, respectively (Figs. 8, 9). Generally, aftershocks typically occur around the mainshock rupture area, and they may also activate nearby-faults due to stress changes induced by the mainshock. In first order approximation the relocated aftershock activity delineates a planar structure trending SW-NE that is dipping towards the NNW, consistent with the geometry of the Karadere fault (Fig. 9). The plane best fitting to the seismicity (contained within 1 km distance) has a strike of $\varphi = 257°$ and a shallow dip of approximately $\delta = 45°$ (Fig. 9). The strike of this plane is thus in good agreement with the moment tensor solutions for the M_W 6.0 mainshock (Table S2). However, the dip of our plane is shallower than the $\delta^{fm} = 72° - 82°$ reported by the moment tensor solutions (Fig. 9c). The depth of the seismicity along the strike of the fault segment is not uniform, with the southwestern portion of the fault displaying generally shallower seismicity from 5 to 13 km depth, and the northeastern portion of the activated fault between 9 and 16 km depth (Fig 9b). Along strike, the hypocentral location of the mainshock coincides with this depth change, suggesting the presence of a fault jog or a heterogeneity that could have promoted a stress concentration.

The mainshock triggered an aftershock sequence that within the first six days can be fitted with an Omori law of the shape $N(t) = kt^{-p}$, with p = 0.90 and k = 2.5 (see Fig S8). Typical values observed for the p-value representing the decay rate oscillate around 1.0, suggesting that the aftershock decay associated with this sequence is fairly standard, including 3-4 M_W > 4 earthquakes occurring within the analyzed time window.

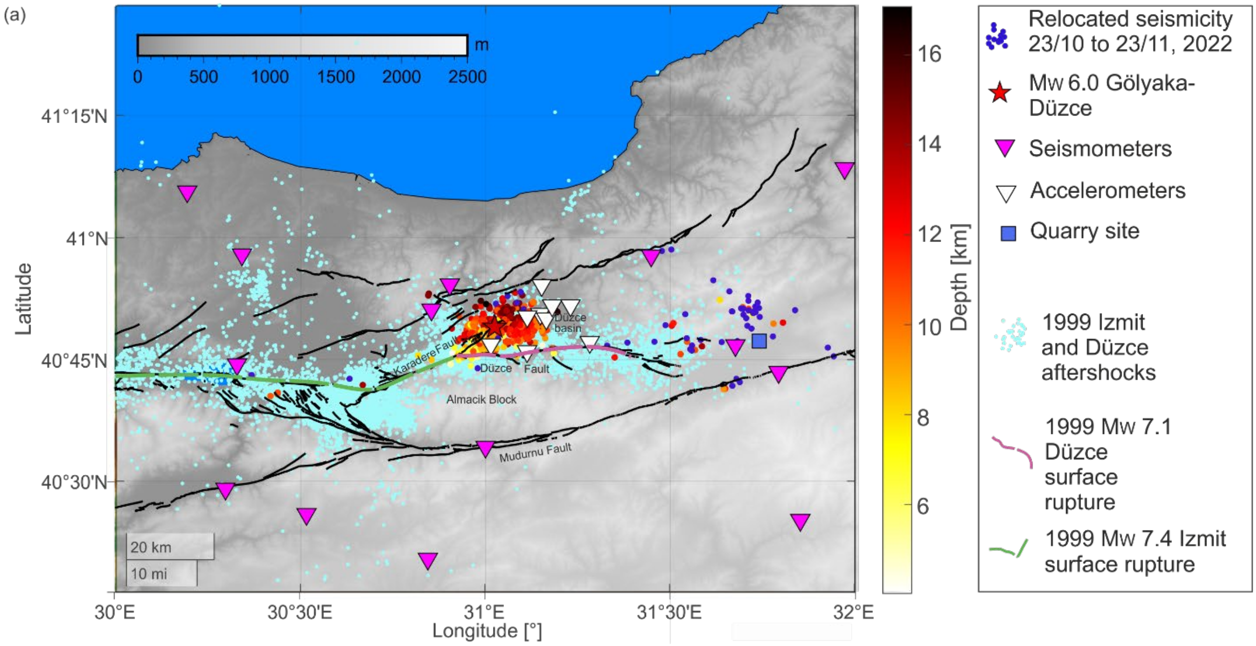

Figure 8: Seismicity distribution after the Gölyaka-Düzce earthquake *(colored dots). Cyan dots in the background reflect 1999 Izmit and Düzce aftershocks. For comparison, seismic activity for three different time periods around the 1999 Izmit and Düzce mainshock is shown (from Bohnhoff et al, 2016b, Bulut et al., 2005).*

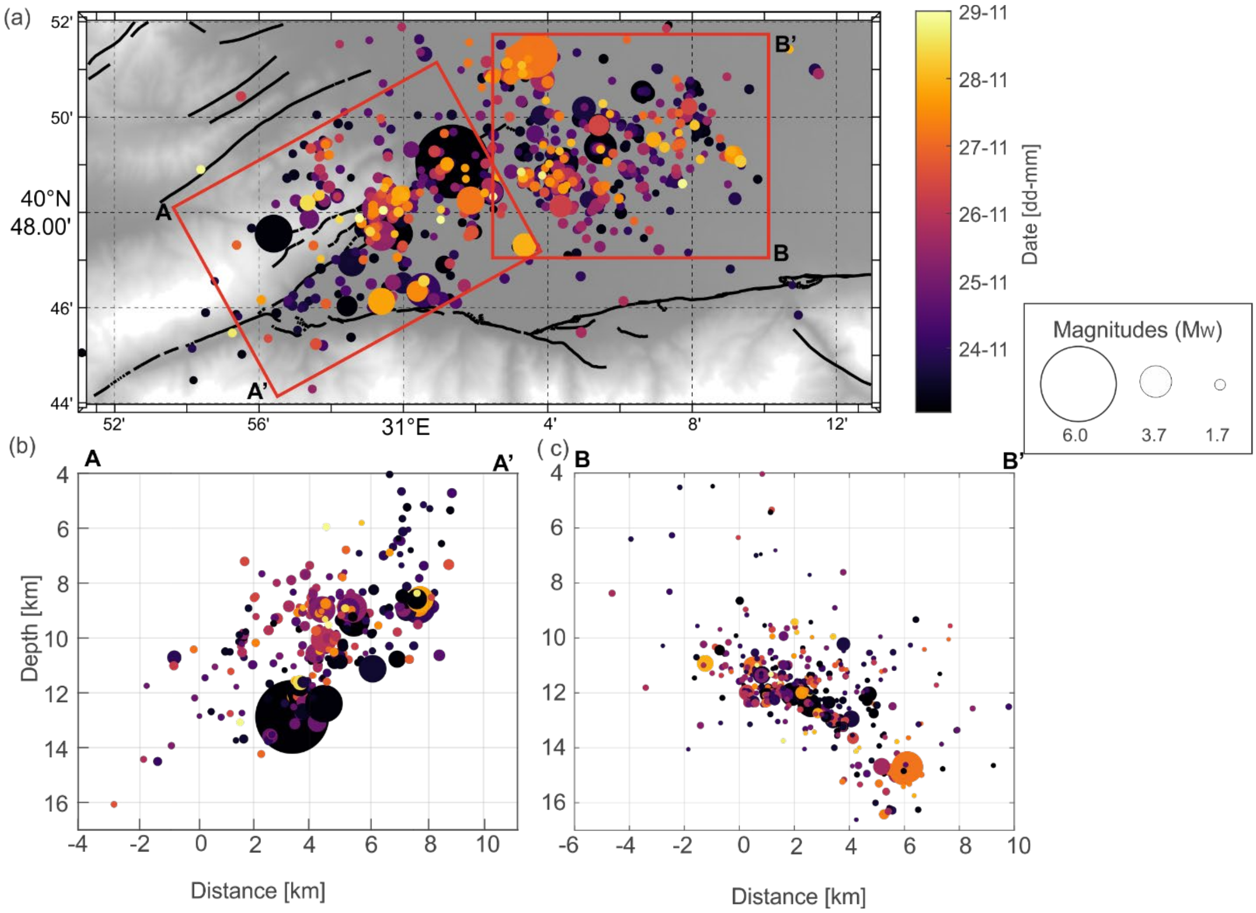

Figure 9: Zoom on the spatio-temporal distribution of the seismicity during 6 days following the Gölyaka-Düzce earthquake. *(a) Map view. Depth profiles along (b) A- A' (approximately perpendicular to the Karadere fault strike), and (c) B-B' (approximately perpendicular to the strike of the Düzce fault). Symbol size and color are encoded with magnitude and date, respectively.*

3.3 Source parameters and directivity of the Gölyaka-Düzce mainshock

Earthquake source parameters for the 2022 M_W 6.0 Gölyaka-Düzce mainshock are provided in Table 1, with the average values and multiplicative error factors calculated in log10 domain (García-García et al., 2004). The averaged seismic moment is 8.80×10^{17}, leading to a moment magnitude of Mw 5.9, equal to the moment magnitude given by AFAD. The average corner frequency f_c values obtained for P and S-waves are 0.23 Hz and 0.24 Hz, respectively, with a ratio of $\frac{f_{cP}}{f_{cS}} = 0.96$. The obtained ratio of corner frequencies from P- and S- waves is lower than the $\frac{V_P}{V_S} = 1.73$, which holds for a stationary source and can be decreased due to the rupture propagation effects (Sato and Hirasawa, 1973; Kwiatek and Ben-Zion 2013). In general, the $f_{cP} > f_{cS}$ arises for roughly equidimensional source models (L=W). While for long and thin faults, lower $\frac{f_{cP}}{f_{cS}}$ ratios are to be expected; for example, $\frac{f_{cP}}{f_{cS}} = 0.77$ assuming rupture velocity $V_R = 0.9V_S$ (Savage et al., 1972); nearly equal f_{cP} and f_{cS} are given in a dislocation model with a unilateral rupture propagation (Haskell, 1964, Molnar et al., 1973). The small f_{cP}/f_{cS} ratio might imply that the fault width W could be overestimated from the aftershock distribution and could be smaller than 8 km, which is also supported by the narrower fault width estimated from the early aftershock distribution (Fig. 9).

Attenuation greatly affects the amplitude and frequencies included in the seismograms. Commonly, S waves tend to have larger attenuation than P waves. The ratio between the P and S quality factors is:

$$\frac{Q_P}{Q_S} = \frac{3}{4}\frac{V_P^2}{V_S^2}. \qquad (18)$$

For a Poisson solid, $V_P = \sqrt{3}V_S$, resulting in $\frac{Q_P}{Q_S}$=2.25. Our observations provide a considerably lower $\frac{Q_P}{Q_S}$=1.2. Such lower ratios are not uncommon and have been interpreted as the attenuating effect of pore fluids (Olsen et al., 2003; Hauksson and Shearer, 2006; Kwiatek et al., 2013, 2015).

Utilizing the average source size and seismic moment from both P- and S-waves, the static stress drop of the mainshock is estimated as 0.61 MPa and 1.48 MPa while using a Brune model (Eq 12), and a Haskell model, respectively (Table 1). The estimated rupture length varies around 14 km and 6 km for Brune and Haskell model, which yields a rectangular source with a small L/W ratio. A relatively small aspect ratio was also observed for the M_W 1999 7.1 in direct vicinity of this area (Bürgmann et al., 2002).

Fig. 10 shows P-wave arrivals highlighting the initial portion of the ground displacement record Δt. Longer Δt rise times and durations of first P-wave displacement pulses are observed for western stations with azimuth angles of 196°-293°(i.e., stations SUSU, GEYV, KAYN and KAND). At the same time, eastern stations at comparable distances and azimuth angles ranging 32°-130° display shorter rise times and visibly higher frequency content (see discussion in Douglas et al., 1988, Fig. 10b), especially for station RUZG and BCAM near 90° azimuth. These observations suggest eastwards rupture propagation while assuming a unilateral rupture. However, in the case of a more complicated rupture process, the shorter rise time could also be promoted by a closer large-local slip asperity in the eastern direction. We also estimated the azimuthal variations on the f_c for the stations between 200 km and 800 km from the mainshock. (Fig S9). Larger f_c values are observed at approximately 100°, hence being roughly consistent with the eastward rupture propagation. However, we note that scattered large f_c values were also observed at other azimuths.

Table 1. ***Source parameters for the 2022 M_W 6.0 Gölyaka-Düzce earthquake***. *f_c: Corner frequency. M_0: Seismic moment. L: Source rupture length. Q: Quality factor. Δσ: Stress drop.*

	Average value	**Multiplicative error factor**
M_0 (N m)	8.80×10^{17}	2.60
f_{cP} (Hz)	0.23	1.51
f_{cS} (Hz)	0.24	1.52
Q_P	571	1.52
Q_S	476	1.28
L_{Brune} (km)	14.26	1.66
$L_{Haskell}$ (km)	5.90	1.63
$\Delta\sigma_{Brune}$ (MPa)	0.61	2.60
$\Delta\sigma_{Haskell}$ (MPa)	1.48	2.93

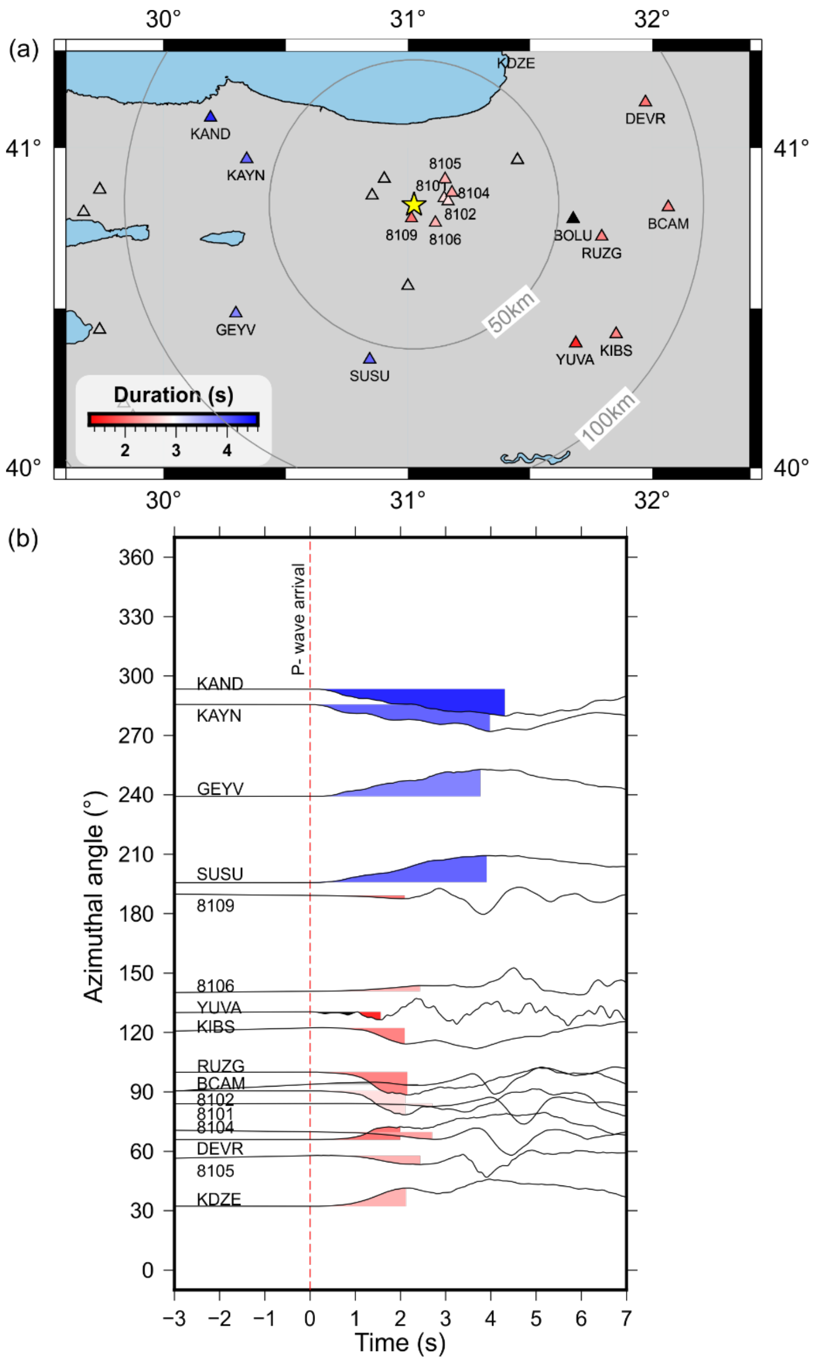

Figure 10: First-peak duration recorded at seismic stations between 50 km and 100 km from the mainshock epicenter. *(a) Station distribution near the epicenter (yellow star). Colored triangles highlight the stations used in (b). (b) Normalized displacement recordings on radial components. The waveforms are aligned relative to the P-wave arrival (0 s) in the time axis and are ordered according to the azimuthal angles relative to the mainshock. The time duration of the colored segments is shown color-coded for in the station symbols in (a).*

4 Discussion

The various spatio-temporal scales covered by the different methodologies applied in this study provide insights into the processes leading to and involved in the rupture of the M_W 6.0 Gölyaka-Düzce earthquake. In the following, we discuss the most important patterns that emerged from the obtained results, as well as their relation with the rheology of the region, the development of previous large earthquakes (i.e. the $M > 7$ Izmit and Düzce earthquakes), and its stage in the seismic cycle.

4.1 The 1999 $M > 7$ Izmit and Düzce earthquakes promoted the seismic activation of the Karadere fault

The Karadere fault connects the Akyazi and Düzce basins, which are both pull-apart structures in response to the regional transtensional tectonic setting (Pucci et al., 2006; Ickrath et al., 2015; Bohnhoff et al., 2016b). The spatio-temporal evolution of seismicity along different portions of the broader Marmara region since 1990 shows that the Karadere fault was primarily quiet until the occurrence of the 1999 M>7 Izmit and Düzce events (Fig 5). Most of the Karadere fault was activated during the 1999 August 17th, M_W 7.4 Izmit earthquake while its northeastern portion likely hosted fewer aftershocks (Bohnhoff et al., 2016b). The 1999 Izmit rupture was then extended further eastwards 87 days later with the 1999 November 11th M_W 7.1 Düzce earthquake onto the east-west trending Düzce fault splaying off the Karadere fault, and also dipping towards the North with a dip of around 55° (Bürgmann et al., 2002).

The November 23th 2022 M_W 6.0 Gölyaka-Düzce rupture likely occurred on the northeastern portion of the Karadere fault that remained inactive in 1999, marking the western flank of the Düzce Basin as a topographic depression north of the Düzce fault as a releasing bend. The fact that the Izmit rupture stopped on the Karadere fault and redirected onto the Düzce fault indicates that the northeastern Karadere fault acted as a barrier in 1999. This is supported by the observation of a lower seismic velocity contrast in the Karadere fault with respect to the fault regions west of it (e.g. the Mudurnu fault, see Najdamahdi et al., 2016). Nevertheless, our results show increased background seismic activity from 1999 onwards in the Karadere segment, with a visible increase in 2004-2005. One hypothesis is that the stress redistribution from the 1999 Izmit and Düzce earthquake sequences brought the Karadere segment closer to failure by stress transfer, leading to a progressive activation of this segment over the years. That way, after 23 years of additional continuous tectonic loading, it was finally activated with a M_W 6 event within a region of the fault zone that it still is in a relatively early phase of the seismic cycle. Some support for this scenario comes from a reported change in stress regime together with a rotation of the S_{hmin} orientation in the Karadere segment before and after the 1999 Izmit and Düzce sequences (Ickrath et al., 2015). Before the earthquakes, a predominantly normal faulting stress regime was observed, while strike-slip regime was observed after the Düzce earthquake. As the magnitude of S_V at a certain depth is mostly given by the weight of the overburden, it is expected to remain approximately constant during the earthquake cycle. This suggest that the horizontal shear stresses on the fault increased after the 1999 sequence. We additionally note that the average recurrence period of M > 7 earthquakes in area is around 250 years (Murru et al., 2016). Therefore, the recurrence time of a M > 6 earthquake should be about 25 years, which roughly fits with the occurrence of the last M > 7 earthquakes 23 years before the Gölyaka-Düzce event.

The observed changes in the background seismicity rates could also be related to a change in the seismic coupling of the region (e.g. Marsan et al., 2017; Jara et al., 2017). In particular, the occurrence of the 1999 $M > 7$ Izmit and Düzce earthquakes and their post seismic deformation could have resulted in promoting the occurrence of aseismic slip at depth, hence leading to a progressive decoupling of the fault. The build-up of stresses from the occurrence of enhanced aseismic slip can increase the background seismicity rates over the region with distributed deformation over a large area. Indeed, an additional proposed mechanism for the 1999 Düzce rupture was viscoelastic post-seismic relaxation at depth affecting a broad area from the 1999 Izmit rupture (e.g. Bürgmann et al., 2002; Ergintav et al., 2009). A detailed study on the microseismicity from this area also suggested that this possibility could account for the larger seismicity rates at depths (Beaucé et al, 2022).

4.2 How did the mainshock start?

Our catalog of absolute locations revealed at least 23 seismic events with epicentral location less than 25 km from the M_W 6.0 Gölyaka-Düzce during the month before its occurrence. Out of them, only two are located in the north eastern segment of the Karadere Fault, as the main fault segment that ruptured in the Gölyaka-Düzce event. The spatio-temporal evolution of these events does not suggest clustering, but rather a scattered activation of the area (Fig S7).

Likewise, the foreshocks do not generally resemble a spatial or temporal localization of the seismicity prior to the mainshock. This is of relevance since a number of moderate to large earthquakes in this region displayed systematic foreshock activity (Bouchon et al., 2011; Ellsworth and Bulut, 2018; Malin et al., 2018; Durand et al., 2020). A similarly spatio-temporally scattered precursory activity pattern as for the mainshock was also found for the 1999 M_W 7.1 Düzce earthquake, where the largest event in the region of the earthquake rupture in the preceding 65 h was a M 2.6 event (Wu et al., 2013). Additional small events detected around the future Düzce 1999 rupture did not show any clear signatures of acceleration. The few seismic events preceding the 2022 M_W 6.0 event, together with their lack of spatio-temporal localization suggest the existence of relatively homogenous local stress conditions along this fault segment, or alternatively, homogeneous fault strength, that would allow a progressive fault loading without rupturing small heterogeneities in the medium reflecting foreshock activity. In this respect, laboratory rock deformation experiments have shown that seismic precursors are more frequent on rough fault surfaces, while seismic foreshocks are much less frequent on polished fault surfaces (Dresen et al., 2020). This is consistent with the linear and relatively simple geometry of the eastern portion of the Karadere segment. In fact, the decade-long seismicity along the Karadere fault shows that it is notoriously more localized within the fault trace than in other fault areas (see e.g. Wu et al., 2013).

The fault area that was activated in the 1999 $M > 7$ Izmit and Düzce earthquakes is documented to continue displaying post-seismic deformation almost 20 years after (Ergintav et al., 2009, Aslan et al., 2019), mainly related to afterslip and viscoelastic relaxation. In this respect, one possibility is that the initiation of the mainshock was also promoted by the occurrence of distributed aseismic slip in the region at depth over a broad area (e.g. Beaucé et al., 2022; Karabulut et al., 2022). This is supported by the observation of a small number of seismic events around November 11th, at the bottom of the Düzce fault, near the place where the 1999 Düzce earthquake nucleated (Fig 6).

Another hypothesis is that a regional or local stress perturbation could have destabilized the northeastern Karadere fault that was close to failure. Some examples for such a potential stress perturbation may include tidal effects or seasonal effects such as the effect of precipitation (e.g. Hainzl et al., 2013) or barometric pressure changes (Martínez-Garzón et al., 2023). Regarding seasonal or semi-periodic stress perturbations, it is worth to mention that the M_W 6.0 Gölyaka earthquake, a M_W 4.9 event in 2021 as the largest and most recent event in this area, and the 1999 M_W 7.1 occurred within the second half of November. Further statistical analysis is not conducted in the frame of this study, but may give further indication on whether earthquakes in this region show any significant temporal pattern.

4.3 Fault segments potentially activated during the mainshock and aftershock sequence

Based on the estimated rupture length from the mainshock source parameters, the event activated a ~12 km long segment of the Karadere fault, terminating just east of the Düzce Basin (Fig 9). Although we tested the application of EGf methods to recover the directivity more accurately, the analysis did not yield clear results (see Text S1 for details). The reasons for this are not clear. It may be that the events used for the EGF deconvolution did not fulfill all necessary criteria (e.g. occurring on the same location, similar focal mechanism and at least a unit of magnitude difference). Alternatively, it could be that the mainshock rupture did not activate a single fault segment, resulting in some complexity obscuring the directivity pattern.

The rupture complexity is also somewhat consistent with the spatial distribution of aftershock seismicity, which shows a heterogeneous event distribution, possibly also illuminating fault structures that were not directly involved in the mainshock rupture. On the western section, the spatial distribution of aftershock seismicity is oriented SE, and part of the distribution suggests the activation of a NW-dipping fault plane of the mainshock in accordance with fault-plane solutions of the event (Table S2), as well as with the size of the mainshock rupture estimated from source parameters.

However, the eastern part of the aftershock distribution is also compatible with the fault geometry of the main Düzce fault activated in 1999. Indeed, the main cluster of events is located at approximately 10 km distance from the mapped surface trace of the Düzce fault. As the deepest aftershock seismicity is located at about 15 km depth, the distribution is also consistent with a fault dipping at about 55°, as we previously reported in Section 3.2.2 (Fig 9). Indeed, this dip is more consistent with the fault geometry reported for the Düzce fault (Bürgmann et al., 2002) than with the dip of the Karadere fault extracted from the focal mechanism of the M_W 6.0 Gölyaka-Düzce earthquake.

Therefore, we suggest that the aftershock distribution that we obtained is likely reflecting the activation of both faults, the Karadere segment displaying a steeper dip towards the northwest, as observed from the focal mechanisms, and the main Düzce fault at depth dipping more gently (around 55°) towards the north.

4.4 A proxy for rupture directivity suggests a larger radiation of energy towards the East

Higher frequency P-wave pulses with shorter rise times were identified in the eastward seismic stations from the rupture, suggesting that the mainshock propagated towards the East. A statistically-preferred rupture propagation towards the East was also resolved in the Karadere fault segment below 5 km depth based on the analysis of fault-zone head waves (FZHW) and fault-zone reflected waves (FZRW) (Najdahmadi et al., 2016). At depth, the authors identified the faster side being the elevated crustal Almacik block to the SW. Together with models of bimaterial ruptures, these results suggest that earthquakes on the Karadere segment nucleating at > 5 km depth have a physically explainable preferred propagation direction to the east. However, at shallower depth the fault core was detected to host even slower material between both blocks to either side (Najdahmadi et al., 2016). This led the authors to conclude on a narrow wedge-shaped structure of the fault rather than a simple first-order impedance contrast of the fault. A preferred rupture propagation towards the East was also resolved in the Mudurnu Fault segment (about 70 km West of the mainshock epicenter, see Fig. 6) from detection of fault zone head waves (Bulut et al., 2012). From the moveout of the fault zone head waves, a velocity contrast of about 6% was estimated, with a slower seismic velocity for the northern side of the fault. An eastward propagation of the rupture was also reported for the 1999 M_W 7.1 Düzce earthquake rupture from the joint analysis of geodetic, seismic and strong motion data (Konca et al., 2010). We conclude that based on our observations of an eastward-directed rupture during the Mw 6.0 Gölyaka-Düzce earthquake, the observations of the fault-zone head waves in the region and existence of bimaterial faults in the area should be considered an important ingredient for refined seismic risk studies in the area, especially for the Istanbul metropolitan region further to the West. However, this only applies if earthquakes are located along the bimaterial interface. For earthquakes located on secondary splay faults or in the rock volume, their rupture directivities may be related to other factors. A future possible analysis of the source parameters from the smaller events of the sequence may reveal whether the eastward directivity is a persistent feature in the region.

5 Conclusions

We investigated the source parameters of the 2022 M_W 6.0 Gölyaka earthquake in NW Türkiye, as well as the evolution of the seismicity framing this mainshock at various spatial and temporal scales. This earthquake mainly ruptured the Karadere fault, a small fault segment located in direct vicinity of the 1999 M_W 7.1 Düzce earthquake. Hence, this case is an example of a medium size earthquake which ruptured a critically stressed fault embedded in a fault zone that is overall in a relatively early stage of the seismic cycle. Our primary goal was to determine how the earthquake initiated, what are the ongoing deformation mechanisms in the region, and how the energy from this mainshock was radiated. The main conclusions extracted from our analysis are the following:

(1) The decade-long evolution of background seismicity in the Karadere segment shows that the segment was mostly silent before the 1999 $M > 7$ Izmit and Düzce earthquakes. From the year 2000 to present, the segment has been comparatively more seismically active, supporting the hypothesis of a progressive approach to critical stress level of the fault segment.

(2) The high-resolution seismicity catalogs derived in this study report on 23 locatable events during the previous month within a 25 km radius from the 2022 Gölyaka-Düzce earthquake. Only few of them occurred close to the future earthquake rupture, suggesting relatively homogenous fault stress conditions and no signatures of foreshock localization were observed.

(3) The early aftershocks of the sequence (i.e. first six days) suggested activation of the Karadere fault segment dipping steeply towards the NW as reported by the moment tensor, and the Düzce fault in the southern part dipping shallower directly towards the North. This suggests that the mainshock rupture, located along the Karadere fault, was able to trigger abundant aftershocks in the neighboring fault segment.

(4) Analysis of mainshock rupture directivity patterns including an attempt to employ empirical Green's functions analysis did not yield clear results. However, shorter rise time and higher frequency content of the P-wave pulses is observed at seismic stations located East of the mainshock hypocenter. If the mainshock rupture did indeed show promoted directivity towards the East, the observation is consistent with predictions from models of bimaterial interfaces and observations from fault zone head waves at this fault.

Author contribution

PMG and DB generated the enhanced seismicity catalog, JJ analyzed the long-term seismicity rate variations, XC estimated the stress drop, EGF and directivity estimations using methodologies developed previously by GK, all authors discussed the results in terms of the seismo-tectonic setting, PMG drafted the manuscript and all co-authors contributed to its finalization.

Acknowledgments

We thank Elif Turker and Fabrice Cotton for discussions and comparison with their directivity results from ground motion. P.M.G. and D.B. acknowledge funding from the Helmholtz Association in the frame of the Young Investigators Group VH-NG-1232 (SAIDAN). X. C. acknowledges funding from the Deutsche Forschungs Gemeinschaft (DFG) in the frame of the proposal "Earthquake source characterization and directivity effects near Istanbul: Implications for seismic hazard".

Open Research

Seismicity catalogs generated in this study with Artificial intelligence are being prepared for public release through the repository of the GFZ Data Services (link in preparation). While this is being prepared, we provide the three catalogs developed here within the submission files.

Seismicity catalogs from AFAD and KOERI agencies are available under the landing websites https://tdvms.afad.gov.tr/ (last accessed 29/08/2023) and http://www.koeri.boun.edu.tr/sismo/2/earthquake-catalog/ (last accessed 29/08/2023), respectively. The here generated AFAD and KOERI catalogs correspond to the time period from October 23rd, 2022 at 00:00h up to November 29th, 2022 at 00:00h. Longitude and latitude ranges of 30°-32°, and 40°-41°, respectively.

Competing interests

The authors declare no conflict of interests.

References

Abercrombie, R. E. (1995). Earthquake source scaling relationships from− 1 to 5 ML using seismograms recorded at 2.5-km depth. *Journal of Geophysical Research: Solid Earth*, *100*(B12), 24015-24036.

Ambraseys, N. N. (1970). Some characteristic features of the Anatolian fault zone. *Tectonophysics*, *9*(2–3), 143–165. htps://doi.org/10.1016/0040-1951(70)90014-4

Ambraseys, N. N., & Zatopek, A. (1969). The Mudurnu Valley, West Anatolia, Turkey, earthquake of 22 July 1967. *Bulletin of the Seismological Society of America*, *59*(2), 521–589. https://doi.org/10.1785/BSSA0590020521

Aslan, G., Lasserre, C., Cakir, Z., Ergintav, S., Özarpaci, S., Dogan, U., et al. (2019). Shallow Creep Along the 1999 Izmit Earthquake Rupture (Turkey) From GPS and High Temporal Resolution Interferometric Synthetic Aperture Radar Data (2011–2017). *Journal of*

Geophysical Research: Solid Earth, *124*(2), 2218–2236. https://doi.org/10.1029/2018JB017022

Beaucé, E., van der Hilst, R. D., & Campillo, M. (2022). Microseismic Constraints on the Mechanical State of the North Anatolian Fault Zone 13 Years After the 1999 M7.4 Izmit Earthquake. *Journal of Geophysical Research: Solid Earth*, *127*(9), e2022JB024416. https://doi.org/10.1029/2022JB024416

Bilham, R., Ozener, H., Mencin, D., Dogru, A., Ergintav, S., Cakir, Z., Aytun, A., Aktug, B., Yilmaz, O., Johnson, W., & Mattioli, G. (2016). Surface creep on the North Anatolian Fault at Ismetpasa, Turkey, 1944-2016. *Journal of Geophysical Research: Solid Earth*, *121*(10), 7409–7431. https://doi.org/10.1002/2016JB013394

Bohnhoff, M., Martínez-Garzón, P., Bulut, F., Stierle, E., & Ben-Zion, Y. (2016a). Maximum earthquake magnitudes along different sections of the North Anatolian fault zone. *Tectonophysics*, *674*, 147–165. https://doi.org/10.1016/j.tecto.2016.02.028

Bohnhoff, M., Ickrath, M., & Dresen, G. (2016b). Seismicity distribution in conjunction with spatiotemporal variations of coseismic slip and postseismic creep along the combined 1999 Izmit-Düzce rupture. *Tectonophysics*, *686*, 132–145. https://doi.org/10.1016/j.tecto.2016.07.029

Boore, D. M., and J. Boatwright (1984), Average body-wave correction coefficients, Bull. Seismol. Soc. Am., 74, 1615–1621.

Bouchon, M. (2002). Space and Time Evolution of Rupture and Faulting during the 1999 Izmit (Turkey) Earthquake. *Bulletin of the Seismological Society of America*, *92*(1), 256–266. https://doi.org/10.1785/0120000845

Bouchon, M., Karabulut, H., Aktar, M., Özalaybey, S., Schmittbuhl, J., & Bouin, M.-P. (2011). Extended Nucleation of the 1999 Mw 7.6 Izmit Earthquake. *Science*, *331*(6019), 877–880. https://doi.org/10.1126/science.1197341

Bouin, M. P., Bouchon, M., Karabulut, H., & Aktar, M. (2004). Rupture process of the 1999 November 12 Düzce (Turkey) earthquake deduced from strong motion and Global Positioning System measurements. *Geophysical Journal International*, *159*(1), 207–211. https://doi.org/10.1111/j.1365-246X.2004.02367.x

Bürgmann, R., Ayhan, M. E., Fielding, E. J., Wright, T. J., McClusky, S., Aktug, B., et al. (2002). Deformation during the 12 November 1999 Düzce, Turkey, Earthquake, from GPS and InSAR Data. *Bulletin of the Seismological Society of America*, *92*(1), 161–171. https://doi.org/10.1785/0120000834

Bulut, F., Ben-Zion, Y., & Bohnhoff, M. (2012). Evidence for a bimaterial interface along the Mudurnu segment of the North Anatolian Fault Zone from polarization analysis of P waves. *Earth and Planetary Science Letters*, *327–328*, 17–22. https://doi.org/10.1016/j.epsl.2012.02.001

Bulut, F., Özener, H., Doğru, A., Aktuğ, B., & Yaltırak, C. (2018). Structural setting along the Western North Anatolian Fault and its influence on the 2014 North Aegean Earthquake (Mw 6.9). *Tectonophysics*, *745*(July), 382–394.https://doi.org/10.1016/j.tecto.2018.07.006

Cakir, Z., Akoglu, A., Belabbes, S., Ergintav, S., & Meghraoui, M. (2005). Creeping along the Ismetpasa section of the North Anatolian fault (Western Turkey): Rate and extent from InSAR. *Earth and Planetary Science Letters*, *238*(1–2), 225–234.https://doi.org/10.1016/j.epsl.2005.06.044

Cetin, E., Cakir, Z., Meghraoui, M., Ergintav, S., & Akoglu, A. M. (2014). Extent and distribution of aseismic slip on the Ismetpaşa segment of the North Anatolian Fault (Turkey) from Persistent Scatterer InSAR. *Geochemistry, Geophysics, Geosystems*, *15*(7), 2883–2894. https://doi.org/10.1002/2014GC005307

Daniel, G., Marsan, D., & Bouchon, M. (2008). Earthquake triggering in southern Iceland following the June 2000 Ms6.6 doublet. *Journal of Geophysical Research: Solid Earth*,*113*(5). https://doi.org/10.1029/2007JB005107

Delouis, B., P. Lundgren, and D. Giardini. 2004. Slip distributions of the 1999 Dücze (Mw 7.2) and Izmit (Mw 7.6) earthquakes on the North Anatolian Fault (Turkey): A combined analysis. internal report, 2004

Di Bona, M., & Rovelli, A. (1988). Effects of the bandwidth limitation of stress drops estimated from integrals of the ground motion. *Bulletin of the Seismological Society of America*, *78*(5), 1818-1825.

Douglas, A., Hudson, J. A., & Pearce, R. G. (1988). Directivity and the Doppler effect. *Bulletin of the Seismological Society of America*, *78*(3), 1367-1372.

Durand, V., Bentz, S., Kwiatek, G., Dresen, G., Wollin, C., Heidbach, O., et al. (2020). A Two-Scale Preparation Phase Preceded an Mw 5.8 Earthquake in the Sea of Marmara Offshore Istanbul, Turkey. *Seismological Research Letters*, *91*(6), 3139–3147. https://doi.org/10.1785/0220200110

Dziewonski, A. M., T.-A. Chou, & J. H. Woodhouse (1981), Determination of earthquake source parameters from waveform data for studies of global and regional seismicity, J. Geophys. Res., 86, 2825-2852, doi:10.1029/JB086iB04p02825.

Ekström, G., M. Nettles, & A. M. Dziewonski (2012), The global CMT project 2004-2010: Centroid-moment tensors for 13,017 earthquakes, *Phys. Earth Planet. Inter.*, 200-201, 1-9, doi:10.1016/j.pepi.2012.04.002.

van der Elst, N. J., & Shaw, B. E. (2015). Larger aftershocks happen farther away: Nonseparability of magnitude and spatial distributions of aftershocks. *GeophysicalResearch Letters*, *42*(14), 5771–5778.

Ellsworth, W. L., & Bulut, F. (2018). Nucleation of the 1999 Izmit earthquake by a triggered cascade of foreshocks. *Nature Geoscience*, *11*(7), 531. https://doi.org/10.1038/s41561-018-0145-1

Ergintav, S., McClusky, S., Hearn, E., Reilinger, R., Cakmak, R., Herring, T., et al. (2009). Seven years of postseismic deformation following the 1999, M = 7.4 and M = 7.2, Izmit-Düzce, Turkey earthquake sequence. *Journal of Geophysical Research: Solid Earth*, *114*(B7). https://doi.org/10.1029/2008JB006021

Eyidoğan, H., 2022, What happened in Düzce? A preliminary assessment of the November 23 quake in Western Turkey, Temblor, http://doi.org/10.32858/temblor.291

García-García, J., M. Romacho, and A. Jiménez (2004), Determination ofnear-surface attenuation, withκparameter, to obtain the seismic moment,stress drop, source dimension and seismic energy for microearthquakes inthe Granada Basin (Southern Spain),Phys. Earth Planet. Inter.,141(1),9–26, doi:10.1016/j.pepi.2003.08.00

Görgün, E., Bohnhoff, M., Bulut, F., & Dresen, G. (2010). Seismotectonic setting of the Karadere–Düzce branch of the North Anatolian Fault Zone between the 1999 Izmit and Düzce ruptures from analysis of Izmit aftershock focal mechanisms. *Tectonophysics*, *482*(1–4), 170–181. https://doi.org/10.1016/j.tecto.2009.07.012

Gulia, L., & Wiemer, S. (2019). Real-time discrimination of earthquake foreshocks and aftershocks. *Nature*, *574*(7777), 193–199. https://doi.org/10.1038/s41586-019-1606-4

Hanks, T. C., & Kanamori, H. (1979). A moment magnitude scale. *Journal of Geophysical Research: Solid Earth*, *84*(B5), 2348-2350.

Hainzl, S., Ben-Zion, Y., Cattania, C., & Wassermann, J. (2013). Testing atmospheric and tidal earthquake triggering at Mt. Hochstaufen, Germany. *Journal of Geophysical Research: Solid Earth*, *118*(10), 5442–5452. https://doi.org/10.1002/jgrb.50387

Haskell, N. A. (1964), Total energy and energy density of elastic wave radiation from propagating faults, Bull. Seismol. Soc. Am., 54, 1811–1841.

Hauksson, E., & Shearer, P. M. (2006). Attenuation models (QP and QS) in three dimensions of the southern California crust: Inferred fluid saturation at seismogenic depths. *Journal of Geophysical Research: Solid Earth*, *111*(B5).

Ickrath, M., Bohnhoff, M., Dresen, G., Martínez-Garzón, P., Bulut, F., Kwiatek, G., & Germer, O. (2015). Detailed analysis of spatiotemporal variations of the stress field orientation along the Izmit-Düzce rupture in NW Turkey from inversion of first-motion polarity data. *Geophysical Journal International*, *202*(3), 2120–2132. https://doi.org/10.1093/gji/ggv27

Irmak, T. S., Yavuz, E., Livaoğlu, H., Şentürk, E., & Sahin, E. Y. (2020). Source parameters for small-moderate earthquakes in Marmara Region (Turkey). *Geosciences Journal*, *24*(5), 541–555. https://doi.org/10.1007/s12303-019-0039-2

Jara, J., Socquet, A., Marsan, D., & Bouchon, M. (2017). Long-Term Interactions Between Intermediate Depth and Shallow Seismicity in North Chile Subduction Zone. *Geophysical Research Letters*, *44*(18), 9283–9292. https://Oagadoi.org/10.1002/2017GL075029

Jolivet, R., Jara, J., Dalaison, M., Rouet-Leduc, B., Özdemir, A., Dogan, U., Çakir, Z., Ergintav, S., & Dubernet, P. (2023). Daily to Centennial Behavior of Aseismic Slip Along the Central Section of the North Anatolian Fault. Journal of Geophysical Research: Solid Earth, 128(7), 1–35. https://doi.org/10.1029/2022JB026018

Karabulut, H., Bouchon, M., & Schmittbuhl, J. (2022). Synchronization of small-scale seismic clusters reveals large-scale plate deformation. *Earth, Planets and Space*, *74*(1). https://doi.org/10.1186/s40623-022-01725-z

Kadirioğlu, F. T., & Kartal, R. F. (2016). The new empirical magnitude conversion relations using an improved earthquake catalogue for Turkey and its near vicinity (1900–2012). *Turkish Journal of Earth Sciences*, *25*(4), 300–310. https://doi.org/10.3906/yer-1511-7

Konca, A. O., Leprince, S., Avouac, J.-P., & Helmberger, D. V. (2010). Rupture Process of the 1999 Mw 7.1 Duzce Earthquake from Joint Analysis of SPOT, GPS, InSAR, Strong-Motion, and Teleseismic Data: A Supershear Rupture with Variable Rupture Velocity. *Bulletin of the Seismological Society of America*, *100*(1), 267–288. https://doi.org/10.1785/0120090072

Kurt, A. I., Özbakir, A. D., Cingöz, A., Ergintav, S., Doğan, U., & Özarpaci, S. (2022). Contemporary velocity field for Turkey inferred from combination of a dense network of long term GNSS observations. *Turkish Journal of Earth Sciences*, *31*. https://doi.org/10.55730/yer-2203-13

Kwiatek, G., Plenkers, K., Dresen, G., & JAGUARS Research Group. (2011). Source parameters of picoseismicity recorded at Mponeng deep gold mine, South Africa: Implications for scaling relations. Bulletin of the Seismological Society of America, 101(6), 2592-2608.

Kwiatek, G., and Y. Ben-Zion (2013), Assessment of P and S wave energy radiated from very small shear-tensile seismic events in a deep South African mine, J. Geophys. Res. Solid Earth, 118, 3630–3641, doi:10.1002/jgrb.50274.

Kwiatek, G., Martínez-Garzón, P., Dresen, G., Bohnhoff, M., Sone, H., & Hartline, C. (2015). Effects of long-term fluid injection on induced seismicity parameters and maximum magnitude in northwestern part of The Geysers geothermal field. *Journal of Geophysical Research: Solid Earth*, *120*(10), 7085-7101.

Kwiatek, G., and Y. Ben-Zion (2016), Theoretical limits on detection and analysis of small earthquakes, J. Geophys. Res. Solid Earth, 121, 5898–5916, doi:10.1002/2016JB012908.

Le Pichon, X., Şengör, C., Kende, J., İmren, C., Henry, P., Grall, C., & Karabulut, H. (2015). Propagation of a strike slip plate boundary within an extensional environment: the westward propagation of the North Anatolian Fault. *Canadian Journal of Earth Sciences*. https://doi.org/10.1139/cjes-2015-0129

Lomax, A., J. Virieux, P. Volant, & C. Berge (2000), Probabilistic earthquake location in 3D and layered models: Introduction of a Metropolis-Gibbs method and comparison with linear locations, in *Advances in Seismic Event Location* Thurber, C.H., and N. Rabinowitz (eds.), Kluwer, Amsterdam, 101-134.

Lomax, A., Michelini, A., & Curtis, A. (2009), Earthquake Location, Direct, Global-Search Methods, in Complexity In *Encyclopedia of Complexity and System Science*, Part 5, Springer, New York, pp. 2449-2473, doi:10.1007/978-0-387-30440-3.

Malin, P. E., Bohnhoff, M., Blümle, F., Dresen, G., Martínez-Garzón, P., Nurlu, M., et al. (2018). Microearthquakes preceding a M4.2 Earthquake Offshore Istanbul. *Scientific Reports*, *8*(1), 16176. https://doi.org/10.1038/s41598-018-34563-9

Martínez-Garzón, P., Bohnhoff, M., Ben-Zion, Y., & Dresen, G. (2015). Scaling of maximum observed magnitudes with geometrical and stress properties of strike-slip faults. *Geophysical Research Letters*, 2015GL066478. https://doi.org/10.1002/2015GL066478

Martínez-Garzón, P., Beroza, G. C., Bocchini, G. M., & Bohnhoff, M. (n.d.). Sea level changes affect seismicity rates in a hydrothermal system near Istanbul. *Geophysical Research Letters*, *n/a*(n/a), e2022GL101258. https://doi.org/10.1029/2022GL101258

Molnar, P., Tucker, B. E., & Brune, J. N. (1973). Corner frequencies of P and S waves and models of earthquake sources. *Bulletin of the Seismological Society of America*, *63*(6-1), 2091-2104.

Murru, M., Akinci, A., Falcone, G., Pucci, S., Console, R., & Parsons, T. (2016). M ≥ 7 earthquake rupture forecast and time-dependent probability for the sea of Marmara region, Turkey. *Journal of Geophysical Research: Solid Earth*, 2015JB012595. https://doi.org/10.1002/2015JB012595

Najdahmadi, B., Bohnhoff, M., & Ben-Zion, Y. (2016). Bimaterial interfaces at the Karadere segment of the North Anatolian Fault, northwestern Turkey. *Journal of Geophysical Research: Solid Earth*, *121*(2), 2015JB012601. https://doi.org/10.1002/2015JB012601

Ogata, Y. (1988). Statistical Models for Earthquake Occurrences and Residual Analysis for Point Processes. *Journal of the American Statistical Association*, *83*(401), 9–27.https://doi.org/10.1080/01621459.1988.10478560

Ogata, Y., & Katsura, K. (1993). Analysis of temporal and spatial heterogeneity of magnitude frequency distribution inferred from earthquake catalogues. *Geophysical Journal International*, *113*(3), 727–738. https://doi.org/10.1111/j.1365-246X.1993.tb04663.x

Özalp, S. and Kürçer, A., 2022. 23 Kasım 2022 Gölyaka (Düzce) Depremi (Mw 6,0) Saha Gözlemleri ve Değerlendirme Raporu, MTA Jeoloji Etütleri Dairesi Başkanlığı, Ankara, Türkiye, 30 s. (*in Turkish*)

Pucci, S., Pantosti, D., Barchi,M., Palyvos, N., 2006. Evolution and complexity of the seismogenic Düzce fault zone (Turkey) depicted by coseismic ruptures, Plio-Quaternary structural pattern and geomorphology. Geophys. Res. Abstr. 8 08339).

Raub, C., Martínez-Garzón, P., Kwiatek, G., Bohnhoff, M., & Dresen, G. (2017). Variations of seismic b-value at different stages of the seismic cycle along the North Anatolian Fault Zone in northwestern Turkey. *Tectonophysics*, *712–713*, 232–248. https://doi.org/10.1016/j.tecto.2017.05.028

Ross, Z. E., Cochran, E. S., Trugman, D. T., & Smith, J. D. (2020). 3D fault architecture controls the dynamism of earthquake swarms. *Science*, *368*(6497), 1357–1361. https://doi.org/10.1126/science.abb0779

Sato, T., and T. Hirasawa (1973), Body wave spectra from propagating shear cracks, *J. Phys. Earth,* 21, 415–432.

Stirling, M. W., Wesnousky, S. G., & Shimazaki, K. (1996). Fault trace complexity, cumulative slip, and the shape of the magnitude-frequency distribution for strike-slip faults: a global survey. *Geophysical Journal International*, *124*(3), 833–868. https://doi.org/10.1111/j.1365-246X.1996.tb05641.x

Olsen, K. B., Day, S. M., & Bradley, C. R. (2003). Estimation of Q for long-period (> 2 sec) waves in the Los Angeles basin. *Bulletin of the Seismological Society of America*, *93*(2), 627-638.

Salvatier, J., Wiecki, T. V., & Fonnesbeck, C. (2016). Probabilistic programming in Python using PyMC3. *PeerJ Computer Science*, *2*(4), e55. https://doi.org/10.7717/peerjcs.55

Sengör, A. M. C. (2005). The North Anatolian Fault: a new look. *Ann. Rev. Earth Panet. Sci.*, *33*, 37–112.

Snoke, J. A. (1987). Stable determination of (Brune) stress drops. *Bulletin of the Seismological Society of America*, *77*(2), 530-538.

Stein, S., & Wysession, M. (2009). *An introduction to seismology, earthquakes, and earth structure*. John Wiley & Sons.

Stierle, E., Vavryčuk, V., Šílený, J., & Bohnhoff, M. (2014). Resolution of non-double-couple components in the seismic moment tensor using regional networks—I: a synthetic case study. *Geophysical Journal International*, *196*(3), 1869–1877. https://doi.org/10.1093/gji/ggt502

Tibi, R., Bock, G., Xia, Y., Baumbach, M., Grosser, H., Milkereit, C., et al. (2001). Rupture processes of the 1999 August 17 Izmit and November 12 Düzce (Turkey) earthquakes. *Geophysical Journal International*, *144*(2), F1–F7. https://doi.org/10.1046/j.1365-246x.2001.00360.x

Utsu, T., & Seki, A. (1954). A relation between the area of after-shock region and the energy of main-shock. *Journal of the Seismological Society of Japan*, *7*, 233–240.https://doi.org/10.4294/zisin1948.7.4233

Waldhauser F., & Ellsworth, W.L. (2000), A double-difference earthquake location algorithm: Method and application to the northern Hayward fault, *Bull. Seism. Soc. Am.*, 90, 1353-1368.

Waldhauser F, Ellsworth W.L., Schaff, D.P., & Cole, A. (2004), Streaks, multiplets, and holes: high-resolution spatiotemporal behavior of Parkfield seismicity. *Geophys. Res. Lett.*,31, no. 18, doi: 10.1029/2004GL020649.

Wesnousky, S. G. (1988). Seismological and structural evolution of strike-slip faults. *Nature*, *335*(6188), 340–343. https://doi.org/10.1038/335340a0

Wiemer, S., Gerstenberger, M., & Hauksson, E. (2002). Properties of the Aftershock Sequence of the 1999 Mw 7.1 Hector Mine Earthquake: Implications for Aftershock Hazard. *Bulletin of the Seismological Society of America*, *92*(4), 1227–1240. https://doi.org/10.1785/0120000914

Wu, C., Meng, X., Peng, Z., & Ben-Zion, Y. (2013). Lack of Spatiotemporal Localization of Foreshocks before the 1999 Mw 7.1 Düzce, Turkey, Earthquake. *Bulletin of the Seismological Society of America*, *104*(1), 560–566. https://doi.org/10.1785/0120130140